ELECTROCHEMISTRY. GENERATION AND STORAGE
OF ENERGY FROM RENEWABLE SOURCES

The Synthesis of $ZnMn_2O_4$ by Glycine Nitrate Combustion and an Examination of Its Electrochemical Properties in Aqueous Solutions of $ZnCl_2$ and $NaNO_3$[1]

J. Senćanski[a],*, N. Nikolić[b], S. Blagojević[a],**, M. Marinković[a], and I. Stojković Simatović[c],***

[a] *University of Belgrade, Institute of General and Physical Chemistry, Belgrade, 11158 Republic of Serbia*
[b] *University of Belgrade, Institute for Multidisciplinary Research, Belgrade, 11030 Republic of Serbia*
[c] *University of Belgrade, Faculty of Physical Chemistry, Belgrade, 11158 Republic of Serbia*
* e-mail: sencanskijelena@yahoo.com
** e-mail: sblagojevic@iofh.bg.ac.rs
*** e-mail: ivana@ffh.bg.ac.rs

Abstract—To research potential replacements for $LiMn_2O_4$, this work carries out a synthesis of $ZnMn_2O_4$ (ZMO) through the glycine-nitrate combustion. XRPD validates its phase characterization; electron microscopy confirmed the presence of single phase ZMO in the form of curvy and rod-shaped sub-micron sized particles at an average of 113 nm. This work is novel for its electrochemical measurements of ZMO as a cathodic material for alkali-ion batteries, performed by cyclic voltammetry in aqueous solutions of $ZnCl_2$ and $NaNO_3$ ranging from 5 to 100 mV s^{-1} polarization rates, yielding stable capacities for both electrolytes. The highest capacities were obtained for the polarization speed of 5 mV s^{-1} for both electrolytes. Their cathode capacities were 11.3 and 27.2 mA h g^{-1} for $ZnCl_2$ and $NaNO_3$, respectively. Concerning Na-ions batteries, the surface storage is the deciding factor due to the adsorption of Na$^+$ ions on the λ-MnO_2 phase. Unlike Zn-ions, Na$^+$ ions cannot intercalate into the spinel structured materials.

INTRODUCTION

Zn is widely used in disposable alkaline batteries and may also be a potential component of cathode materials used to replace those existing in Li-ion batteries. Current materials used in Li-battery cathodes are costly. Zn as a more affordable alternative may be a potential cathode material for the spinel-structure of $LiMn_2O_4$. Other materials common in Li-ion batteries include $LiMnO_2$ [1], $LiMn_2O_4$ [2, 3], $LiNiO_2$ [4, 5], $LiCoO_2$ [4, 6], $LiCo_{1/3}Ni_{1/3}Mn_{1/3}O_2$ [7–10], as well as $LiFePO_4$ [11], components of which may also be potentially replaced with Zn based materials. The organic ethylene carbonate (EC)/dimethyl carbonate (DMC) used in commercial Li-ion batteries is hazardous as it is both toxic and flammable. In order to create a more environmentally friendly battery, there have been multiple attempts to replace an organic electrolyte with an aqueous electrolyte as well as to replace Li ions with Zn or Na ions in a cathode material. Based on intercalation and de-intercalation of Zn-ions into

and from cathode and anode materials, the working principle of Zn-ion batteries is the same as for Li-ion batteries. As cathode materials for Zn-ion batteries, the same materials are used as for Li-ion batteries: the oxides of transition metals.

One of the materials used as a cathode material for Zn-ion batteries is $ZnMn_2O_4$. Shi et al. [12] have performed a synthesis of ZMO doped by $Ti_3C_2T_x$ by the hydrothermal method. The electrochemical properties of the material were examined by cyclic voltammetry as well as galvanostatic charge and discharge including electrochemical impedance spectroscopy as they are the most used methods to test cathodic and anodic materials. The results obtained for ZMO@$Ti_3C_2T_x$ by the galvanostatic charge and discharge method show a high specific capacity of 126 mA h g^{-1} in which the density of the current is 0.1 A g^{-1} and which indicate a high-capacity retention in a gelatin-based aqueous electrolyte. Yang et al. [13] proposed a synthesis of the ZMO through a surfactant-assisted solvothermal method. To examine the material electrochemically, a galvanic charge and discharge was carried out, whose current density was

---

[1] Report at the XV Conference on Physical Chemistry (online), Belgrade, Serbia, September 20–24, 2021.

0.5 A g^{-1}. The initial charge capacity obtained was 15.7 mA h g^{-1} while the initial discharge capacity was 82.6 mA h g^{-1}. The electrolyte used was an aqueous solution of $ZnSO_4$. Another study carried out by Chen et al. [14] carried out a synthesis of the same material but through the hydrothermal method, whose galvanostatic results were 146.9 mA h g^{-1} after 100 cycles at 0.3 A g^{-1}. Yang et al. [15] created the same cathode material through the hydrothermal method, delivering a large reversible capacity of 125.6 mA h g^{-1} at a current density of 1 A g^{-1} after 2000 cycles, yielding a capacity retention of 90.3% in an aqueous solution of $ZnSO_4$ and $MnSO_4$. Zhang et al. [16] examined $ZnMn_2O_4$ as a cathode material in an aqueous solution of $Zn(CF_3SO_3)_2$. Testing the material through the galvanostatic method showed a capacity of 150 mA h g^{-1}, whose retention was 94% after 500 cycles, while its rate was 500 mA g^{-1}.

ZMO has also been used as an anode material. Sekhar et al. [17] carried out an examination of this material as an anode in $NaClO_4$ dissolved in an organic electrolyte. The galvanostatic charge and discharge yielded a capacity of 170 mA h g^{-1} while the rate was 100 mA g^{-1}, whose capacity retention was 1000 cycles. Unlike our work, their synthesis is an example of glycine nitrate combustion whose pH was adjusted to 11. Moreover, to the best of the authors' knowledge, this cathode material has not been synthesized elsewhere in the literature according to the procedure described in the experimental of our work in which the glycine nitrate combustion was used.

A ZMO synthesis was carried out through glycine-nitrate combustion, which was further examined through a phase and morphological analysis. The electrochemical properties of the synthesized ZMO was then examined separately in aqueous solutions of $ZnCl_2$ and $NaNO_3$ salts. Cyclic voltammetry was used to measure the electrochemical characteristics of the synthesized ZMO as it is a fast and simple method to predict the cycling behavior of cathodic and anodic materials.

EXPERIMENTAL

To synthesize $ZnMn_2O_4$, glycine nitrate combustion method was applied. The solutions of 1 M $Mn(NO_3)_2 \cdot 6H_2O$ and $Zn(NO_3)_2 \cdot 6H_2O$ were mixed in a stoichiometric ratio, glycine was then added (glycine/NO_3 = 1.2) and heated at 200°C until complete combustion. It was thereafter air-annealed at 800°C for 4 h.

A Rigaku Ultima IV powder diffractometer using Ni-filtered CuK_α radiation at an interval from 4° to 90° 2θ and a step of 0.02° (scanning rate 2 deg/min) was used to obtain the XRPD data. A Le Bail full-pattern profile fitting method [18], implemented in FullProf software [19], was used for unit cell refinement.

A scanning electron microscope (Tescan VEGA TS 5130MM) operating at 20 kV accelerating voltage was used for the sample morphology analysis.

A Gamry PCI4/300 Potentiostate/Galvanostate at polarization rates from 5 to 100 mV s^{-1} was used to perform the cyclic voltammetry, under a three-electrode system (counter electrode platinum) and reference SCE (saturated calomel electrode). A glossy carbon electrode was used for the working electrode onto which the cathode material was pasted, in a ratio 85 : 10 : 5 of carbon black and polyvinildiendifluoride. The paste was obtained as described in the reference Sencanski et al. [20].

The energy-dispersive spectrometry (EDS) technique using a FEI SCIOS 2 Dual Beam microscope analyzed the chemical composition. The powder was pressed onto copper double-sided adhesive tape and then recorded under a high vacuum with an accelerating voltage of 20 kV.

RESULTS AND DISCUSSION

As shown in Fig. 1a, the XRPD profile was refined using the Le-Bail full profile matching mode in which there were no un-indexed reflections indicating ZMO present as a single phase. The ZMO unit cell was refined to a $I41/amd$ space group under lattice parameters: $a = b = 5.7185(8)$ Å, $c = 9.268(2)$ Å, showing good agreement with the data reported in the literature [21] JCPDS, card no. 24-1133.

The SEM images (Figs. 1b, 1c) show an unexpected morphology for the sol–gel synthesis. Although such a synthesis often yields sponge-like and network-like morphology [22, 23], the synthesized ZMO shows agglomerated, dominantly curly-shaped to less abundant rod-shaped particles. However, at higher magnification, the size of the particles observed are an average of 113 nm. The particle size was determined using SemAfore 5.21 software.

BSE imaging revealed a homogeneous internal microstructure of ZMO particles suggesting particle uniform composition that had no observed exsolutions or additional phases. These, however, could not be determined using XRPD due to the higher detection limit. Due to the submicron-sized particles, a high capacity may be predicted due to the particles' large specific surface area. The results accord with a wide range of similar studies. Chen et al. [14] carried out a synthesis by means of the hydrothermal method where the spheres were 1.3 μm diameter. Moreover, Yang et al. [15] performed a synthesis of the same material by means of the hydrothermal method in which the SEM micrographs showed 20nm particles to have been obtained. The co-precipitation method was applied in Zhang et al. [16] as well, whose SEM micrographs indicated nanoparticles 15 nm on average.

In order to examine the capacity and stability of the material synthesized in this study, cyclic voltammetry
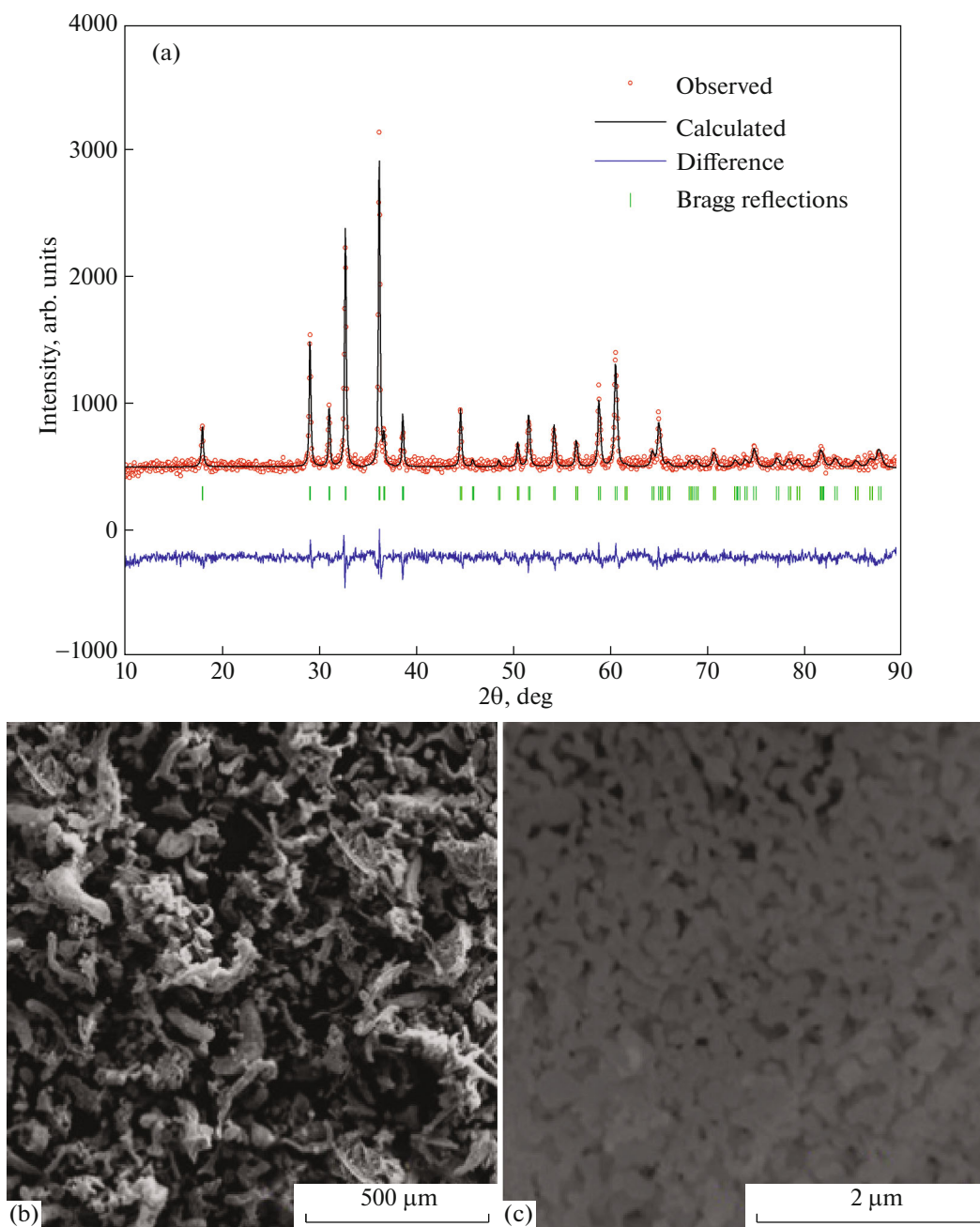
Fig. 1. (a) The experimental and calculated XRPD of the synthesized ZnMn$_2$O$_4$. The red represents the experimental XRPD, the black the calculated XPRD pattern, the blue their differential curve and the green represents the Bragg's positions; (b) secondary-electron (SE), and (c) back-scattered (BSE) images of the synthesized ZnMn$_2$O$_4$.

was performed in aqueous solutions of ZnCl$_2$ and NaNO$_3$ salts. The cyclic voltammograms are presented in Fig. 2 for the polarization rates. As may be observed, for the lower rates, the main anode peak shifted to the higher potentials (from 1.02 to 1.18 V) when the rate increased. Of two cathode peaks observed, the peak at the lower potential shifted to a higher polarization (from 0.74 to 0.78 V), while the peak of the higher potential shifted to lower polariza-

tion (from 0.95 to 0.91 V) when the polarization rate increased. These two peaks merged into a single one when the polarization rate increased at 100 mV s^{-1} (Fig. 2d).

The peaks' separation observed in Fig. 2 shows the main peak positioned at 0.85 V, at a scanning rate of 100 mV s^{-1}. The peaks' positions changed over the de-intercalation and intercalation processes.
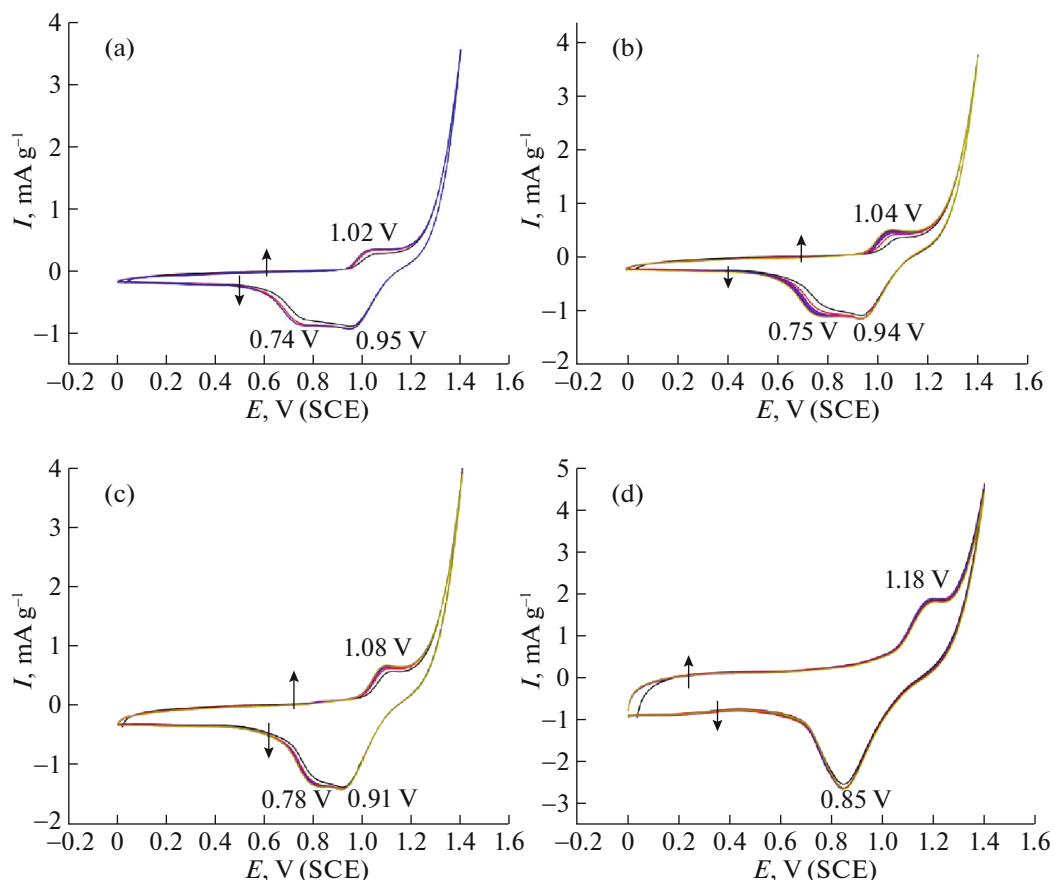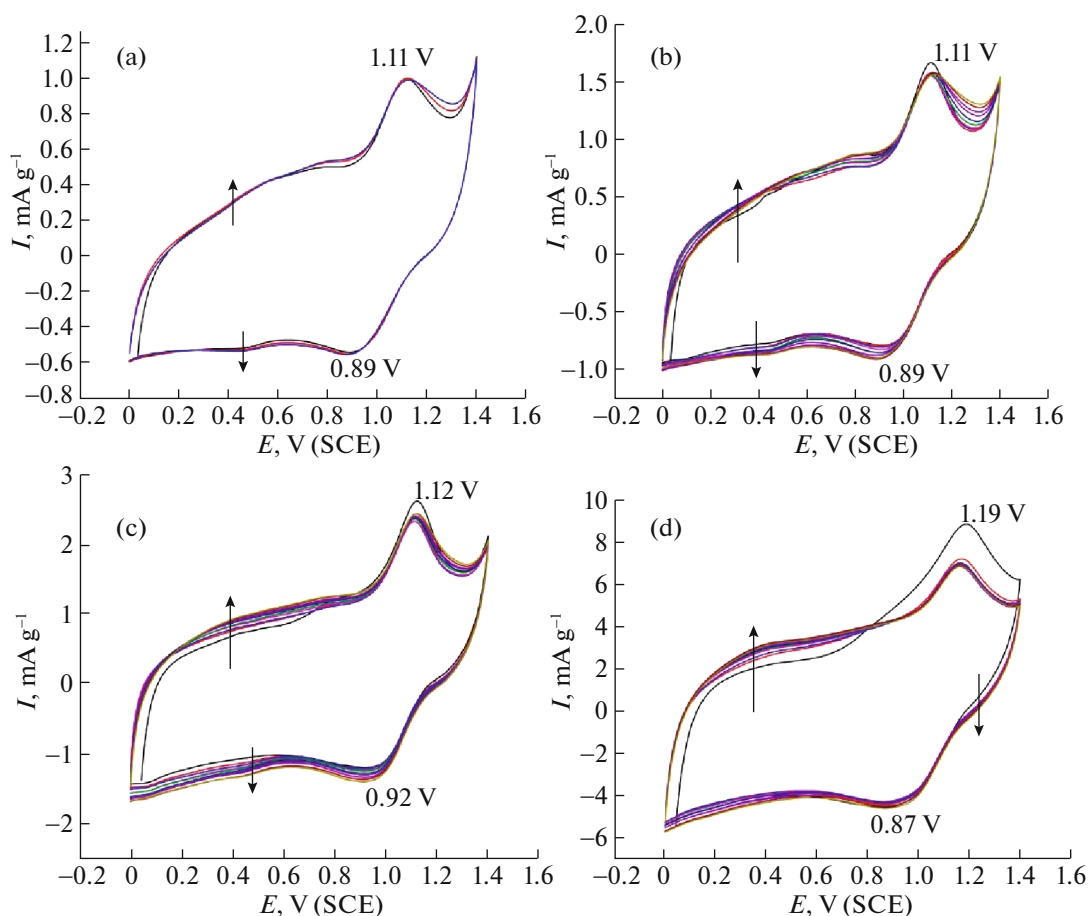
Fig. 2. Cyclic voltammograms of $ZnMn_2O_4$ in an aqueous solution of $ZnCl_2$ at polarization rates of (a) 5, (b) 10, (c) 20, (d) 100 mV s^{-1}. The arrows represent an increase in the cycle number.

In order to examine the electrochemical properties of ZMO in an aqueous solution of sodium salt, a $NaNO_3$ aqueous solution was used to measure its capacity. The same range of polarization rates was applied as for an aqueous solution of $ZnCl_2$. The cyclic voltammograms show a similar pattern and differ from those when an aqueous solution of $ZnCl_2$ was used. There are two main peaks for both the anodic and cathodic cyclic voltammograme (Fig. 3). The values of the anodic and cathodic peaks for 5 and 10 mV s^{-1} hold the same position: 1.11 V for anodic and 0.89 V for cathodic polarization. The peaks' positions for the anode in both the salts are approximately the same for higher rates compared to the distinction observed for lower rates.
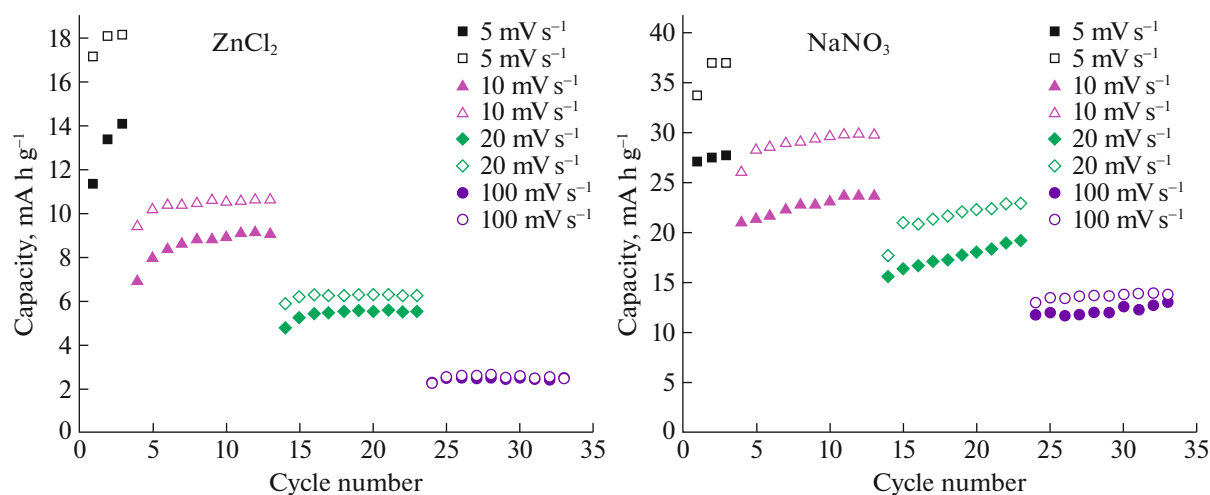
The capacities for aqueous solutions of $ZnCl_2$ and $NaNO_3$, separately, are presented in Fig. 4. The capacity was calculated according to the formula $C = C_1(\text{mA h})/(3600 \times 0.0015g \times 0.85)$, where that obtained was stable for both the aqueous solutions of $ZnCl_2$ and $NaNO_3$, although there was a mild increase. C_1 is the capacity obtained from Gamry Echem Analyst software. As shown in Fig. 4, the

capacities of $ZnCl_2$ were lower for all applied rates compared to those for $NaNO_3$ in terms of both its cathode and anode capacities. The initial anode capacities for an aqueous solution of $ZnCl_2$ were in steps of 17.11, 9.35, 5.87, and 2.21 mA h g^{-1}, while its cathode capacities were 11.3, 6.9, 4.7, and 2.2 mA h g^{-1} respective to the polarization rate increase in steps from 5, 20, 20 to 100 mV s^{-1}. Compared to Zn-ions, the anode initial capacity values in $NaNO_3$ were 33.83, 26.1, 17.72, and 13.04 mA h g^{-1}, while they were 27.2, 21.0, 15.6, and 11.8 mA h g^{-1} for the cathode when the polarization rate was increased at the same respective steps. When the polarization rate was 5 mV s^{-1}, the initial anode capacity for $NaNO_3$ was approximately twofold; while, for the polarization rate of 100 mV s^{-1}, the anode capacity was fourfold. The initial cathode capacity for an aqueous solution of $NaNO_3$ was approximately 1.5 times higher, while it was fourfold times higher for cathode capacity when the polarization rates were 5 and 100 mV s^{-1}.

Due to the impossibility to intercalate Na$^+$ ions into the crystal lattice of the spinel structured material

Fig. 3. Cyclic voltammograms of $ZnMn_2O_4$ in an aqueous solution of $NaNO_3$ at polarization rates of (a) 5, (b) 10, (c) 20, (d) 100 mV s^{-1}. The arrows represent increases in the cycle number.

Fig. 4. The capacity dependence of the scan rate and cycle number in two aqueous solutions. All open symbols represent anode capacities, while the solid symbols represent cathode capacities.

of $ZnMn_2O_4$, XRD, and EDX methods were used to study the principle of storage of Na when cycling the electrode material in a $NaNO_3$ solution. Namely, the

Rietveld refinement of both the initial and after-cycling of the $ZnMn_2O_4$ showed no evidence in structural change either in the unit cell (initial a =
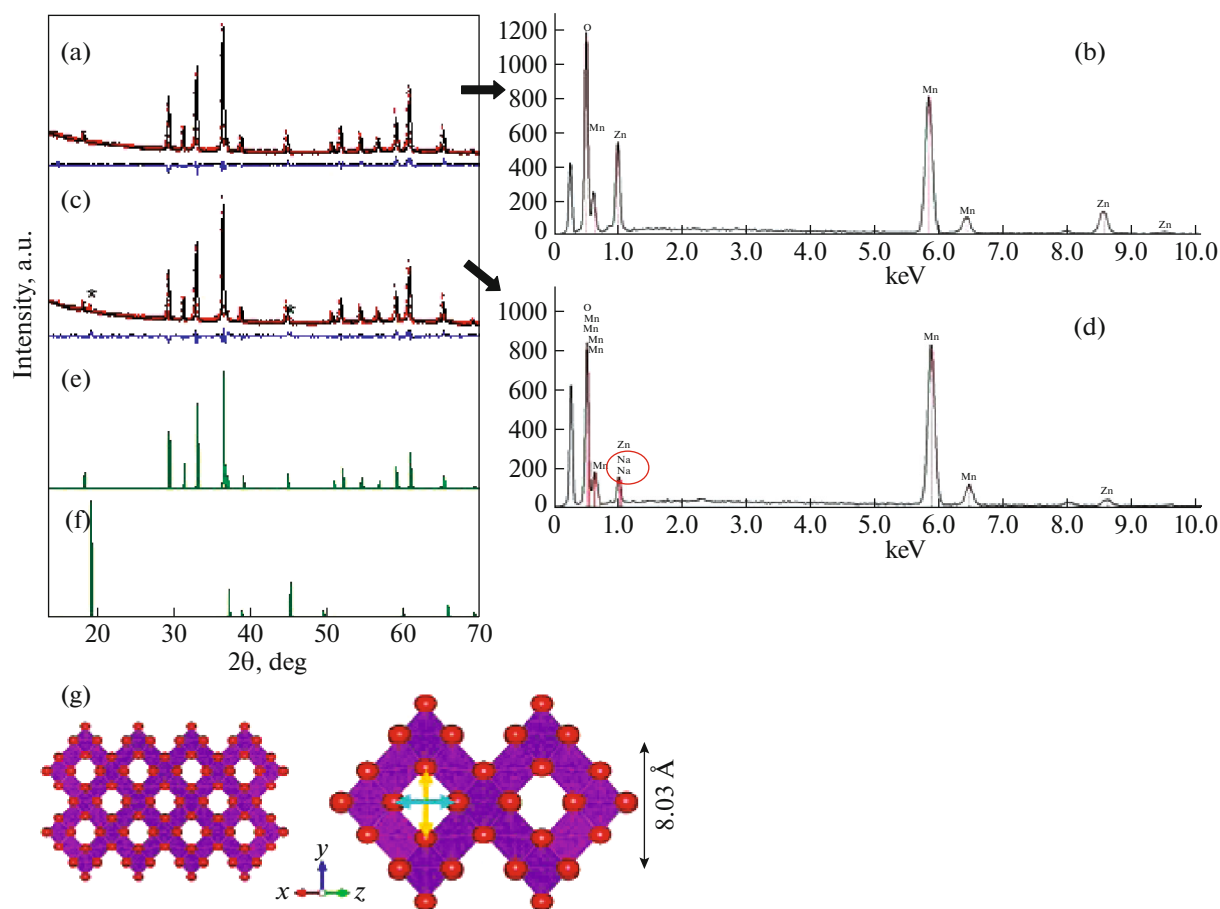
Fig. 5. (a) The Rietveld refined X-ray pattern of the electrode material prior to cycling (red circles−observed data, black line− refined pattern, blue line−differential line); (b) the EDS analysis of electrode material prior to cycling; (c) the Rietveld refined X-ray pattern of electrode material after cycling (red circles−observed data, black line−refined pattern, blue line−differential line) - note that there is an additional diffraction peak at 19.07° and shoulder at 45.15° belonging to λ-MnO$_2$; (d) the EDS analysis of the electrode material after cycling in NaNO$_3$; (e) the ZnMn$_2$O$_4$ X-ray pattern (JCPDS 24-1133); (f) the λ-MnO$_2$ X-ray pattern (JCPDS 44-0992); (g) both the crystal structure of λ-MnO$_2$ along the [110] direction and the unit cell along the [110] direction indicate both rhomb-like tunnels of 3.12294 Å (the pale-blue double arrow) and 4.2253 Å (the yellow double arrow) diagonal dimensions.

5.7186(3) Å, c = 9.2692(9) Å; cycled a = 5.7186(3) Å, c = 9.2677(9) Å) or oxygen position parameters (initial y = 0.518(3), z = 0.242(2); cycled y = 0.518(3), z = 0.243(2)) which appeared identically both in the initial and after-cycling patterns (Figs. 5a and 5c). However, the initial Le Bail full profile matching and Rietveld refinement revealed low additional diffraction peaks at 19.06° and 45.22° in the material after its cycling (Fig. 5c), which are attributable to the cubic λ-MnO$_2$ phase (JCPDS 44-0992) (Fig. 5f). This finding, however, is in line with other results in the literature. According to Hunter [24] and Greedan et al. [25], λ-MnO$_2$ structures are created when Li is removed from LiMn$_2$O$_4$. More recently, Xue et al. [26] have reported results on acid leaching, arguing that Zn^{2+} ions are able to be extracted from the nanocrystal ZnMn$_2$O$_4$ to form a defect spinel of a λ-MnO$_2$ nanocrystal under acidic conditions. The diffraction peak

at ca 19.06° in the cycled-material pattern, indexed as a (111) reflection for the λ-MnO$_2$ phase, slightly increased in a lattice parameter for λ-MnO$_2$ (8.03 Å for pure λ-MnO$_2$, 8.06 Å for studied λ-MnO$_2$), which may indicate that there had been a limited amount of Na incorporated into the λ-MnO$_2$. In order to confirm, it was necessary to carry out an EDS analysis for the electrode material prior to and post cycling in an aqueous solution of NaNO$_3$ in order to demonstrate the mechanism of Na storage in ZnMn$_2$O$_4$. The results obtained suggest the presence of Zn, Mn, and O prior and post cycling, as well as Na after cycling.

Namely, Ooi et al. [27] had conducted more extensive research into the adsorptive properties of λ-MnO$_2$ for mono and divalent metals, including Na, reporting a selectivity sequence of Na$^+$ < K$^+$ < Rb$^+$ < Cs$^+$ ≪ Li$^+$, which showed a remarkably high selectivity for Li

(Kd 104) whose lowest selectivity was for Na (Kd 0.5) in a crystal lattice. Similarly, to the tunnel-like α- and β-MnO_2 modifications, the λ-MnO_2 structure is characterized by a rhomb-like 1 × 3 three-dimensional tunnel structure defined by a MnO_6 octahedra along the [110] direction (Fig. 5g) [28, 29]. The sizes of the cross-section of the ~3.1 and 4.2 Å tunnels are fairly sizable to accommodate even large ions such as Na^+ (1.02 Å). Ooi et al. [27] and later Fang et al. [29] both conducted similar studies on the insertion of Li^+, Na^+ and K^+ into the same structure, concluding that the remarkably larger apparent adsorptive capacity of Li^+ compared to other alkalis are due to the smaller ionic radius of Li^+. Other alkalis which possess larger ionic radii, including Na, suffer a significant steric hindrance and cannot enter vacant tetrahedral sites. They are therefore only adsorbed onto the sites on the crystal surface which are nonspecific for metal ions. In line with Ooi et al. (1987), the low amount of Na detected by EDS in the material after cycling in an aqueous solution of $NaNO_3$ is most likely due to the adsorbed Na^+ ions on the λ-MnO_2 structure surface. Thus such cubic closed-packed $ZnMn_2O_4$ appears not to further participate in the electrochemical reaction in cycling rather than initially acting as a precursor for the formation of λ-MnO_2 phase in the Zn-removal initial charging cycle.

CONCLUSIONS

This work is novel in its research and analysis of glycine nitrate combustion applied to synthesized $ZnMn_2O_4$ for a cathode material used in aqueous Zn-ion and Na-ion batteries. The XRPD refined pattern demonstrates good agreement with the data reported in the literature. The SE/BSE micrographs confirm the particles' submicron-size and dimensions. The electrochemical properties were also examined by cyclic voltammetry, by which a stable capacity was obtained for both electrolytes. However, a higher capacity was obtained for an aqueous solution of $NaNO_3$. The XRD measurements show that the λ-MnO_2 phase is responsible for the Na-ion absorption and surface storage. To increase the capacity of the cathode material, doping the material with another cation or using an aqueous electrolyte containing another salt may be applied.

ACKNOWLEDGMENTS

CONFLICT OF INTEREST

The authors declare that they have no conflicts of interest.

REFERENCES

1. S. Komaba, S. T. Myung, N. Kumagai, et al., Solid State Ionics **152**, 311 (2002).
2. B. J. Hwang, R. Santhanam, and D. G. Liu, J. Power Sources **101**, 86 (2001).
3. N. Cvjeticanin, I. Stojkovic, M. Mitric et al., J. Power Sources **174**, 1117 (2007).
4. J. K. Papp, N. Li, L. A. Kaufman, et al., Electrochim. Acta **368**, 137505 (2021).
5. L. de Biasi, A. Schiele, M. Roca-Ayats, et al., ChemSusChem **12**, 2240 (2019).
6. J. Xu, H. R. Thomas, R. W. Francis, et al., J. Power Sources **177**, 512 (2008).
7. F. Fu, X. G. Wang, L. Qi, et al., J. Mater. Chem. A **1**, 3860 (2013).
8. E. Shinova, R. Stoyanova, E. Zhecheva, et al., Solid State Ionics **179**, 2198 (2008).
9. CM. Julien, A. Mauger, K. Zaghib, et al., Inorganics **2**, 132 (2014).
10. Z. D. Huang, X. M. Liu, S. W. Oh, et al., J. Mater. Chem. **21**, 10777 (2011).
11. J. Molenda and M. Molenda, *Composite Cathode Material for Li-Ion Batteries Based on LiFePO₄ System* (InTech, Rijeka, 2011).
12. M. Shi, B. Wang, Y. Shen, et al., Chem. Eng. J. **399**, 125627 (2020).
13. S. Yang, M. Zhang, X. Wu, et al., J. Electroanal. Chem. **832**, 69 (2019).
14. L. Chen, Z. Yang, H. Qin, et al., Electrochim. Acta **317**, 155 (2019).
15. C. Yang, M. Han, H. Yan, F. Li, et al., J. Power Sources **452**, 227826 (2020).
16. N. Zhang, F. Cheng, Y. Liu, et al., J. Am. Chem. Soc. **138**, 12894 (2016).
17. B. Chandra Sekhar, P. Packiyalakshmi, and N. Kalaiselvi, RSC Adv. **7**, 20057 (2017).
18. A. Le Bail, H. Duroy, and J. L. Fourquet, Mater. Res. Bull. **23**, 447 (1988).
19. J. Rodríguez-Carvajal, Phys. B (Amsterdam, Neth.) **192**, 55 (1993).
20. J. Senćanski, D. Bajuk-Bogdanović, D. Majstorović, et al., J. Power Sources **342**, 690 (2017).
21. Y. Yang, Y. Zhao, L. Xiao, et al., Electrochem. Commun. **10**, 1117 (2008).
22. K. D. Martinson, I. S. Kondrashkova, and V. I. Popkov, Russ. J. Appl. Chem. **90**, 1214 (2017).
23. J. C.Toniolo, M. D. Lima, A. S. Takimi, et al., Mater. Res. Bull. **40**, 561 (2005).
24. C. J. Hunter, J. Solid State Chem. **39**, 142 (1981).
25. J. E Greedan, N. P. Raju, A. S. Wills, et al., Chem. Mater. **10**, 3058 (1998).
26. L. Xue, Z. Wu, C. Ge, et al., Mater. Chem. Phys. **138**, 124 (2013).
27. K. Ooi, Y. Miyai, and S. Katoh, Solvent Extr. Ion Exchange **5**, 561 (1987).
28. K. Ooi, M. Yoshitaka, K. Shunsaku, et al., Langmuir **5**, 150 (1989).
29. F. Qi, K. Hirofumi, Y. Miyai, and K. Ooi, Chem. Mater. **7**, 1226 (1995).